Three-dimensional imaging of strain in a single ZnO nanorod

Marcus C. Newton[1]★†, **Steven J. Leake**[1], **Ross Harder**[2] **and Ian K. Robinson**[1,3]

Nanoscale structures can be highly strained because of confinement effects and the strong influence of their external boundaries. This results in dramatically different electronic, magnetic and optical material properties of considerable utility. Third-generation synchrotron-based coherent X-ray diffraction has emerged as a non-destructive tool for three-dimensional (3D) imaging of strain and defects in crystals that are smaller than the coherence volume, typically a few cubic micrometres, of the available beams that have sufficient flux to reveal the material's structure[1]. Until now, measurements have been possible only at a single Bragg point of a given crystal because of the limited ability to maintain alignment[2]; it has therefore been possible to determine only one component of displacement and not the full strain tensor. Here we report key advances in our fabrication and experimental techniques, which have enabled diffraction patterns to be obtained from six Bragg reflections of the same ZnO nanocrystal for the first time. All three Cartesian components of the ion displacement field, and in turn the full nine-component strain tensor, have thereby been imaged in three dimensions.

The study of nanoscale crystals and structures has intensified as their often unique properties find application in new materials and devices[3–6]. Traditional non-destructive methods such as scanning electron microscopy (SEM), atomic force microscopy and numerous spectroscopic techniques provide detailed information on the surface structure but do not directly probe the structure in the volume as a whole. Transmission electron microscopy is able to provide information on the crystal structure within a material but requires an electron-transparent lamella cross-section for imaging. Such invasive sample preparation can alter the properties of the material, prohibiting further detailed studies. Coherent X-ray diffraction provides detailed information on phase changes in the reflected beam owing to ions displaced from some reference lattice. Coherence is required for interference to occur from all locations within the sample. Diffraction data obtained from such crystals appear as an interference pattern of the intensity distribution centred on each of the reciprocal-space lattice points. Well-faceted crystals produce intensity flares as first predicted by von Laue[7]. Each flare is perpendicular to a respective facet of the crystal. Within the confines of the kinematical approximation and for coherent and monochromatic radiation, the experimentally measured intensity $I(\mathbf{q})$ is related to the scattering amplitude $A(\mathbf{q})$ by $I(\mathbf{q}) = A^*(\mathbf{q})A(\mathbf{q})$. The scattering amplitude is given by $A(\mathbf{q}) = \int d\mathbf{r}\rho(\mathbf{r})e^{-i\mathbf{q}\cdot\mathbf{r}}$ where $\rho(\mathbf{r})$ is the electron density at position $\mathbf{r}$ and $\mathbf{q} = \mathbf{k}_f - \mathbf{k}_i$ is the momentum transfer between incident $\mathbf{k}_i$ and scattered $\mathbf{k}_f$ waves[8]. In the Bragg configuration, waves reflected from an ideal lattice will remain in phase coherence. Ions displaced from the ideal lattice point result in a phase shift of $\phi_i = q_{ij}u_j$ in

the reflected wave from the distorted region where u_j ($j = x, y, z$) is the local ion-displacement vector-component set and $i \in \mathbb{N}_1$ labels the images obtained at different momentum transfer vectors with components q_j. Provided this real-space phase is recovered, a component of the displacement u_j is directly obtained in the direction of the vector with components q_j. Diffraction from multiple Bragg points of the same crystal will therefore provide several components of the displacement vector, from which we can construct the displacement field[9,10]. For an arbitrary number of Bragg points $n > 3$, the problem is in general overdetermined and a regressive approach, such as the 'least-squares' method, is required to construct the displacement field. This is discussed in the Supplementary Information. A special case occurs for $n = 3$ non-coplanar vectors where we can exactly invert the matrix. For the present case of six non-coplanar Bragg points, all three components of the displacement vector u_j are obtained in rectilinear coordinates as

$$u_j = \xi_{ji}q_{ki}\phi_k; \qquad \xi_{ji} = (q_{kj}q_{ki})^{-1} \qquad (1)$$

Here $(q_{kj}q_{ki})^{-1}$ is the inverse matrix of $q_{kj}q_{ki}$ (with units of square length). When using a regressive approach to obtain the displacement vectors u_j, the components of displacement along the vector direction with components q_j for each dataset are unlikely to be entirely consistent owing to errors in the measurement, including statistical noise in the data and alignment procedures used when constructing the displacement field. We can therefore obtain a consistency measure σ_i on each reflection i using the least-squares phase deviation averaged over the image:

$$\sigma_i^2 = \frac{1}{N_0}\sum(\phi_i - q_{ij}u_j)^2 \qquad (2)$$

where N_0 is the total number of voxels and the sum is taken over the entire image. This consistency measure can be separately minimized for each reflection with respect to the arbitrary phase offset inherent in the inversion of the diffraction to an image.

The 'phase problem' occurs in a number of disciplines ranging from X-ray crystallography[11] to astronomy[12] where phase information is lost when only intensity measurements can be made. Various approaches have been taken to solve the classical phase-retrieval problem and have benefited from advances in optimization theory. In our case of a small sized object, the diffraction pattern is bandwidth-limited and hence can be 'oversampled' relative to its Nyquist frequency[13]. The realization that such diffraction patterns can be inverted by iterative algorithms using appropriate constraints to obtain real-space images[14], and the development
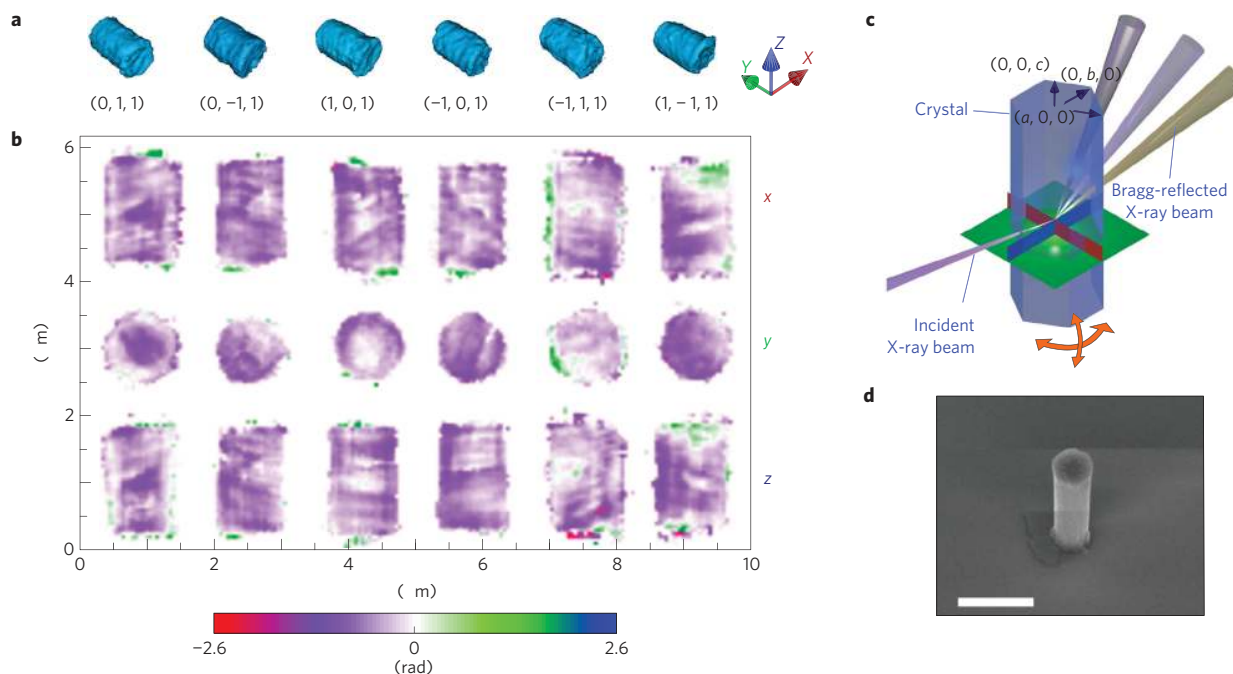
Figure 1 | Reconstructed amplitude and phase of a single ZnO nanorod for six differing Bragg reflections. a, Reconstructed amplitudes shown in isometric projection for each dataset with an 86% isosurface. The crystallographic c axis is aligned along the Cartesian y axis. **b**, Two-dimensional slices of the reconstructed phase maps for each dataset taken from the centre line normal to each axis. A phase range of ± 2.6 rad is used during reconstruction. The phase appears in a range of ± 2.8 rad after recentring (this is discussed in Supplementary Information). **c**, Diagrammatic representation of the experimental conditions in isometric projection showing multiple Bragg reflections from a single ZnO rod. The three planes from which slices of the phase map are taken are also shown. **d**, Scanning electron micrograph of the single ZnO rod used in our X-ray measurements standing on a Si substrate with its c axis approximately normal to the surface. Scale bar: 2 μm.

of efficient phase-retrieval algorithms[15–17], have however made coherent X-ray diffraction microscopy possible. The phase is recovered by traversing back and forth between real and reciprocal space while applying constraints at each iteration. The most effective methods so far apply a real-space constraint that tends to minimize the density outside some predefined 'support' region S within which the object is assumed to exist. The reciprocal-space constraint ensures that the computed modulus $|A(\mathbf{q})|$ is within M, the set of all points with amplitude $\sqrt{I(\mathbf{q})}$, whereas the phase remains unchanged. A solution is found when both conditions are reasonably well satisfied.

ZnO rod-shaped nanocrystals were synthesized through a chemical vapour transport and deposition technique[18] (see the Methods section). Hexagonal-prism-shaped crystals were produced with lengths in the range of 2–4 μm and widths of 1–2 μm. Clean Si substrates were diced into 10×10 mm dies and a cross-shaped mark was scored through the centre of each die. Micromanipulation was used to transfer an individual ZnO rod from the growth substrate to the lower left-hand-side quadrant a few micrometres from the scribed centre region using an optical microscope and a glass-tip needle-shaped manipulation arm. The sample was then heated in pure O_2 at 750 °C for 16 h to grow an oxide layer of 50 nm to secure the crystal in place. After oxidation, the single ZnO rod could be imaged using SEM on the surface, partially embedded into the oxide on the surface (Fig. 1).

Diffraction measurements were made at the Advanced Photon Source beamline 34ID-C. The beam passes through a double-crystal Si monochromator to select a narrow wavelength range centred at 1.42 Å. Diffraction patterns from the (0, 1, 1), (0, −1, 1), (1, 0, 1), (−1, 0, 1), (−1, 1, 1) and (1, −1, 1) reflections were gathered by rotating the sample through the Bragg condition in increments of 0.005°. At each step, two-dimensional (2D) slices of the diffraction pattern were acquired by a direct-detection CCD (charge-coupled

device) with pixel size of 22.5×22.5 μm² and subsequently collated to form a complete 3D diffraction pattern (see Supplementary Fig. S1). As the rod stands perpendicular to the substrate, its (002) reflection is approximately specular. An orientation matrix based on this reflection and one of the (101) reflections was used to set the 34-ID-C diffractometer for each data set. We can immediately deduce some geometric properties of the object before reconstruction using the diffraction pattern alone. By considering the spacing of the fringes normal to and in the six-fold symmetric plane, we can deduce the length and width of the crystal as 2.1 μm and 1.1 μm respectively. The crystal is small enough that the maximum optical-path-length difference is still smaller than the longitudinal coherence length, as confirmed by the full visibility of the fringes seen in each diffraction pattern[19]. Similar results are obtained for all datasets in good agreement with SEM studies. The observation of slight asymmetry in the diffraction data is an indication of the presence of strain in the nanocrystal[20].

Phase reconstruction of the diffraction data was carried out using the phase-constrained hybrid input–output (PC-HIO), error reduction (ER) and phase-only ER algorithms[15,21]. We have also used a custom version of the 'shrink wrap' method, which is used to determine the support region S of the object. Our method is based on the methods used in ref. 22 and was found to provide appreciable improvements in the reconstructed object. The measured intensity $I(\mathbf{q})$ of the sampled diffraction pattern when Fourier transformed provides the autocorrelation function $\rho(-\mathbf{r}) * \rho(\mathbf{r})$ of the object, which we use to obtain an initial estimate of the support. A 2D slice is then taken through the centre of the autocorrelation function (defined at the brightest voxel) and normal to the (001) axis of the crystal. Data below a certain threshold are copied from the slice and subsequently overlaid across a percentage of the autocorrelation function, replacing existing slices, and recentred to the brightest voxel in that slice. The remaining array points were zeroed. Finally,
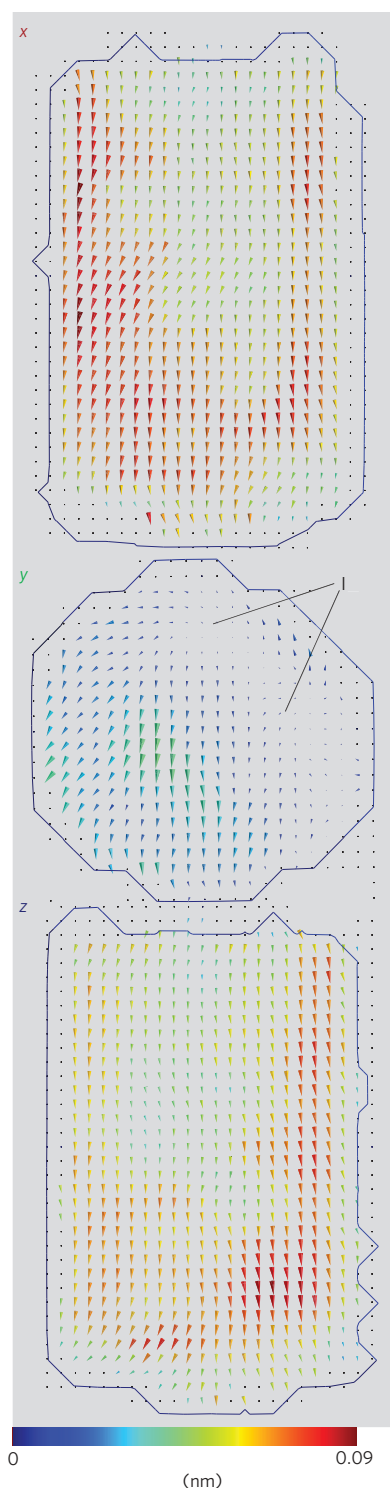
Figure 2 | Two-dimensional slices of the 3D atomic displacement field.
Slices of the ion displacement field taken along the three Cartesian axes according to Fig. 1c. The direction of each arrow indicates the direction of the displacement within the plane. The size of each arrow indicates the magnitude of the displacement. Regions of low displacement are labelled I.

the object is convolved with a moving average and Gaussian function ($\sigma = 0.35$ voxels) to ensure that the support function is compact. The size of the support is controlled by the threshold values selected. Preparing a support in this manner greatly aids the reconstruction of elongated structures, as the support bears some resemblance to an inflated version of the object.

For each dataset, our 'shrink-wrap' procedure starts with 200 iterations of PC-HIO followed by two iterations of ER. A 19.5% threshold of the resulting object was then removed and the object convolved with a moving average and Gaussian function to form an updated support function. Moving-average convolution helps to reduce irregularities such as depressions in the support, whereas convolution with a Gaussian ensures that the new support is always larger than the object by some amount (~10%). A convergence criterion is defined as the difference in the number of voxels that are above a certain threshold between the old and new supports. This process was repeated until convergence was reached at 0.5% of the number of voxels in the support. While the support was converging, the phase reconstruction carried out 40 iterations of PC-HIO and two of ER per cycle. The final image used a further 200 iterations of PC-HIO, and 100 of both ER and phase-only ER with this final support. In the phase-constrained refinements, a phase range of ± 2.6 rad was found to be sufficient to contain the complex density without the occurrence of phase wrapping. After reconstruction, the images were corrected for refraction[2].

The 3D amplitude and 2D cut planes of the real-space phase image for each **q**-vector are shown in Fig. 1. For each reflection, the reconstructed amplitude appears as a rounded crystal with a slight flaring at one end. The length and cross-sectional width of the ZnO rod are in agreement with SEM measurements. Significant phase ripples and shifts can be seen in a number of reconstructions along each of the axial planes. This is more visibly pronounced in the $(0, 1, 1)$ and $(1, -1, 1)$ reconstructions.

The displacement field was calculated using equation (1) after first aligning the amplitudes of each object in real space so that they overlap optimally. By considering the minimum number of fringes visible for each diffraction pattern and the corresponding fringe spacing, we obtain a minimum resolution for constructing the displacement field as 47.3 nm. A correction for the arbitrary phase offset in each dataset was then applied (see Supplementary Information). Each image was transformed by the set of Euler rotations used for the diffractometer setting angles. Spatial alignment is needed because the positions of the objects are not determined by the experiment. Twin images, that is, those that represent a conjugate solution of $\rho^*(-\mathbf{r})$ as opposed to $\rho(\mathbf{r})$ (with identical Fourier transform modulus), are not easily detected for highly symmetric objects. Fortunately, there is a bulge in the crystal shape at one end of the crystal, which is a distinguishing feature that we have used to detect solutions that are twin images. Once this transformation was established, the images were interpolated onto a regular cubic Cartesian grid with a spacing of 50 nm and the displacement vector calculated according to equation (1) at each grid point.

Figure 2 shows the 3D displacement field for the three planes highlighted in Fig. 1. A 3D image of the displacement field can be found in Supplementary Fig. S2. Displacements of up to 0.87 Å are observed. Two regions, labelled I, show displacement vectors an order of magnitude less. Using equation (2) we obtain a consistency σ_i of 0.241, 0.199, 0.263, 0.195, 0.242 and 0.269 rad respectively for each q vector (shown in Fig. 1). From this we can deduce that the $(-1, 1, 1)$ dataset is the least concurrent whereas the $(-1, 0, 1)$ dataset has the best overall agreement.

Having all three orthogonal components of the displacement vector u_i enables us to construct the nine components of the Eulerian strain (ϵ) tensor and rigid-body rotation (τ). In rectilinear co-ordinates we can write these components as

$$\epsilon_{ij} = \frac{1}{2}\left(\frac{\partial u_j}{\partial x_i} + \frac{\partial u_i}{\partial x_j}\right), \qquad \tau_{ij} = \left(\frac{\partial u_j}{\partial x_i} - \frac{\partial u_i}{\partial x_j}\right) \qquad (3)$$

where x_i is the spatial co-ordinate in the orthogonal direction i. Figure 3 shows the resulting strain components calculated using equation (3) and for the three planes highlighted in Fig. 1 (see
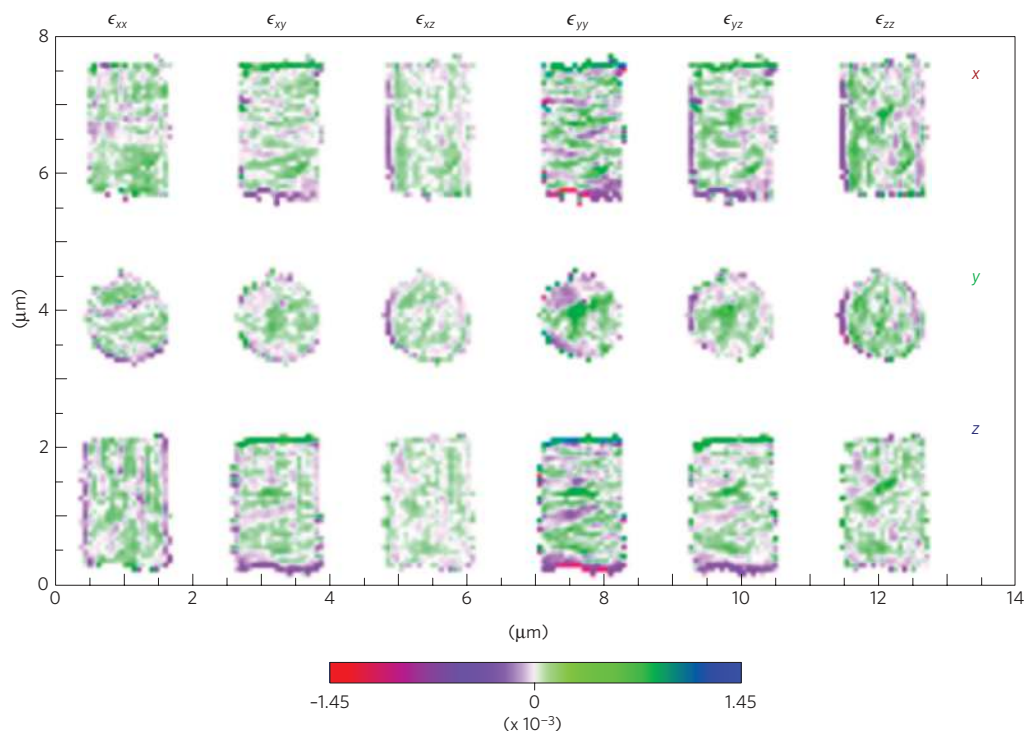
Figure 3 | Two-dimensional slices of the six independent components of the strain tensor. Components are taken along the three Cartesian axes according to Fig. 1c. Regions of compressive (negative) strain are observed near the (100) surfaces of the crystal and at the interface with the Si substrate. A strained layer approximately 200 nm in width near the surface and along the length of the rod (y axis) is visible in all tensor components except the ϵ_{yy} component. This implies that the strain is uniform along the length of the rod. We attribute this to absorption of oxygen at the surface during sample preparation.

Supplementary Fig. S3 for rotation tensor components). The crystallographic c axis (a axis) is aligned along the Cartesian y axis (z axis). Alternating regions of tensile and compressive strain can be seen along the length of the rod with a periodicity of approximately 100 nm. The region of highest compressive strain appears at the base of the crystal where the bulge appears. This might be due to oxygen ion diffusion effects driven by the concentration gradient across the ZnO/Si interface during oxidation[23]. This effect is most obvious in the ϵ_{yy} component. A layer of compressive strain can be seen near the (100) surfaces of the crystal and along the length of the rod, primarily in tensor elements that contain an x or z component. As this is not visible in the ϵ_{yy} component, which is aligned along the crystallographic c axis, this layer of compressive strain is largely continuous along the length of the rod. The observed compressive strain is therefore probably due to relaxation of the $(1, 0, 0)$ lattice spacings as a result of radial oxygen absorption. Oxygen anions diffused into ZnO will reside primarily at interstitial sites, and under our sample-preparation conditions will result in a diffusion-layer thickness of 250 nm (refs 24, 25). Conversely, moderate absorption of certain transition-metal ions and non-metals such as phosphorus are more favourably incorporated into the crystal lattice. Strain in such cases is attributed primarily to differences in the ionic radius of the absorbed species.

Figure 4 shows the strain pattern for a different ZnO crystal prepared for only 1 h in O$_2$. This crystal is lying flat on the substrate surface with the (100) refection approximately specular. Diffraction patterns from the (100) and (010) reflections were gathered, enabling two components of the ion displacement field, and in turn one component (ϵ_{xy}) of the strain tensor, to be imaged in three dimensions. A region of low crystallinity is also visible, labelled I, and is the result of damage arising from manipulation during sample preparation. This effect is not visible in the SEM images, but we note that SEM is not sensitive to the state of
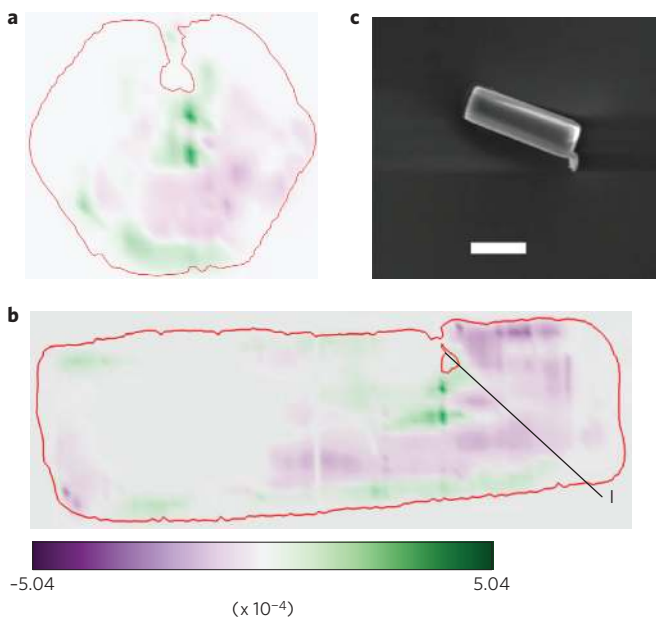

Figure 4 | Strain pattern reconstructed for an extra ZnO nanorod prepared for 1 h in O$_2$. a,b, Cross-sections normal to (**a**) and along (**b**) the crystal c axis of the ϵ_{xy} component of strain are shown. The observation of increased strain at the region of low crystallinity labelled I suggests that some plastic deformation has occurred along the length of the crystal. In contrast to the ZnO crystal subjected to 16 h of O$_2$ at 750 °C in Fig. 1, we do not observe a uniform strain layer along the length of the rod near the surface. The outline shows the 87% isosurface contour of the amplitude. **c,** Scanning electron micrograph image of the single ZnO nanorod. Scale bar: 1 μm.

crystallinity. The impact during sample preparation is likely to have caused some plastic deformation in the vicinity and hence a strain gradient in the surrounding region. Alternating regions of tensile and compressive strain are also visible in the vicinity of the defect with a periodicity of approximately 206 nm. When compared with Fig. 3, it can be seen that there is no obvious layer of strain near the surface and surrounding the crystal. There is however a region of tensile strain towards the base of the rod that might be due to oxygen ion diffusion effects driven by the concentration gradient across the interface with the Si substrate, as described above.

The ability to measure and spatially resolve the full strain tensor within nanoscale crystals has numerous implications for the design of future materials based on nanotechnology. At present our spatial resolution is around 40 nm, but this will improve with better X-ray sources, focussing optics and more stable instrumentation. Possible applications might be band-gap mapping in nanoscale semiconductors, where a transition from indirect to direct band gap has been predicted theoretically[26], or strain engineering of devices for improved carrier mobility. Three-dimensional strain mapping will help understand energy-storage materials. With improved resolution, it may be possible to distinguish the interactions between individual dopant sites through their characteristic strain fields. Last, but not least, the method should be completely practical for imaging transient states in crystals on the femtosecond timescale at future hard-X-ray free-electron-laser sources.

Methods

The synthesis of ZnO hexagonal-prism-shaped nanowires was carried out in a horizontal quartz tube furnace through solid-phase chemical vapour transport and deposition. A crucible containing the source material was placed in the centre of the tube. This consists of a fine mixture of high-purity (99.9999%) 300 mesh graphite and zinc carbonate ($ZnCO_3 \cdot 2Zn(OH)_2 \cdot H_2O$) powder. Si substrates with (111) orientation were cleaned in acetone and propyl alcohol and placed in the downstream region. The system was subsequently purged with 500 s.c.c.m. (standard cubic centimetres per minute) of At carrier gas with an O_2 content of 0.5–5% for 1 h. After this, the tube furnace was heated to 900 °C with the gas flow remaining. Ar 900 °C carbothermal reduction of ZnC released supersaturated Zn, which combines with O_2 to form wurtzite ZnO in the cooler downstream region at 550 °C (ref. 4). The reaction proceeded for 30 min, after which the system was allowed to cool naturally.

References

1. Robinson, I. & Harder, R. Coherent X-ray diffraction imaging of strain at the nanoscale. *Nature Mater.* **8,** 291–298 (2009).
2. Harder, R. *et al*. Orientation variation of surface strain. *Phys. Rev. B* **76,** 115425 (2007).
3. Newton, M. C. & Shaikhaidarov, R. ZnO tetrapod p-n junction diodes. *Appl. Phys. Lett.* **94,** 153112 (2009).
4. Newton, M. C. & Warburton, P. A. ZnO tetrapod nanocrystals. *Mater. Today* **10,** 50–54 (2007).
5. Balili, R., Hartwell, V., Snoke, D., Pfeiffer, L. & West, K. Bose–Einstein condensation of microcavity polaritons in a trap. *Science* **316,** 1007–1010 (2007).
6. Tang, Z. *et al*. Room-temperature ultraviolet laser emission from self-assembled ZnO microcrystallite thin films. *Appl. Phys. Lett.* **72,** 3270–3272 (1998).
7. Laue, M. v. Dieäußere Form der Kristalle in ihrem Einfluß auf die Interferenzerscheinungen an Raumgittern. *Annal. Phys.* **418,** 55–68 (1936).
8. Vartanyants, I. A. & Robinson, I. K. Partial coherence effects on the imaging of small crystals using coherent X-ray diffraction. *J. Phys. Condens. Matter* **13,** 10593–10611 (2001).
9. Pfeifer, M., Williams, G., Vartanyants, I., Harder, R. & Robinson, I. Three-dimensional mapping of a deformation field inside a nanocrystal. *Nature* **442,** 63–66 (2006).
10. Miao, J., Charalambous, P., Kirz, J. & Sayre, D. Extending the methodology of X-ray crystallography to allow imaging of micrometre-sized non-crystalline specimens. *Nature* **400,** 342–344 (1999).
11. Robinson, I. & Miao, J. Three-dimensional coherent X-ray diffraction microscopy. *MRS Bull.* **29,** 177–181 (2004).
12. Fienup, J. R., Marron, J. C., Schulz, T. J. & Seldin, J. H. Hubble space telescope characterized by using phase-retrieval algorithms. *Appl. Opt.* **32,** 1747–1767 (1993).
13. Miao, J., Kirz, J. & Sayre, D. The oversampling phasing method. *Acta Crystallogr. D* **56,** 1312–1315 (2000).
14. Sayre, D. Some implications of a theorem due to Shannon. *Acta Crystallogr.* **5,** 843 (1952).
15. Fienup, J. Phase retrieval algorithms–a comparison. *Appl. Opt.* **21,** 2758–2769 (1982).
16. He, H. *et al*. Inversion of X-ray diffuse scattering to images using prepared objects. *Phys. Rev. B* **67,** 174114 (2003).
17. Barty, A. *et al*. Three-dimensional coherent X-ray diffraction imaging of a ceramic nanofoam: Determination of structural deformation mechanisms. *Phys. Rev. Lett.* **101,** 055501 (2008).
18. Newton, M., Firth, S., Matsuura, T. & Warburton, P. Synthesis and characterization of zinc oxide tetrapod nanocrystals. *J. Phys. Conf. Ser.* **26,** 251–255 (2006).
19. Leake, S. J., Newton, M. C., Harder, R. & Robinson, I. K. Longitudinal coherence function in X-ray imaging of crystals. *Opt. Express* **17,** 15853–15859 (2009).
20. Vartanyants, I., Ern, C., Donner, W., Dosch, H. & Caliebe, W. Strain profiles in epitaxial films from X-ray Bragg diffraction phases. *Appl. Phys. Lett.* **77,** 3929–3931 (2000).
21. Fienup, J. R., Crimmins, T. R. & Holsztynski, W. Reconstruction of the support of an object from the support of its autocorrelation. *J. Opt. Soc. Am.* **72,** 610–624 (1982).
22. Marchesini, S. *et al*. X-ray image reconstruction from a diffraction pattern alone. *Phys. Rev. B* **68,** 140101 (2003).
23. Sabioni, A. C. S., Ramos, M. J. F. & Ferraz, W. B. Oxygen diffusion in pure and doped ZnO. *Mater. Res.* **6,** 173–178 (2003).
24. Philibert, J. Atom movements: Diffusion and mass transport in solids. *Editions Phys.* 5–12 (1991).
25. Erhart, P. & Albe, K. First-principles study of migration mechanisms and diffusion of oxygen in zinc oxide. *Phys. Rev. B* **73,** 115207 (2006).
26. Medaboina, D., Gade, V., Patil, S. K. R. & Khare, S. V. Effect of structure, surface passivation, and doping on the electronic properties of Ge nanowires: A first-principles study. *Phys. Rev. B* **76,** 205327 (2007).

Additional information

The authors declare no competing financial interests. Supplementary information accompanies this paper on www.nature.com/naturematerials. Reprints and permissions information is available online at http://npg.nature.com/reprintsandpermissions. Correspondence and requests for materials should be addressed to M.C.N.